ORIGINAL RESEARCH PAPER

Characterization of Thermal and Electronic Conductivities of Catalyst Layers of Polymer Electrolyte Membrane Fuel Cells

M. Ahadi[1], J. Jankovic[2], M. Tam[2], B. Zahiri[2], M. S. Saha[2], J. Stumper[2], M. Bahrami[1]*

[1] Laboratory for Alternative Energy Conversion (LAEC), School of Mechatronic Systems Engineering, Simon Fraser University, Surrey, BC V3T 0A3, Canada

[2] Automotive Fuel Cell Cooperation Corp., 9000 Glenlyon Parkway, Burnaby, BC, V5J 5J8, Canada

Abstract

This work proposes new and accurate systematic methodologies for *ex situ* measurements of through-plane thermal and in-plane electronic conductivities of catalyst layers (CLs) of polymer electrolyte membrane fuel cells (PEMFC). The developed methods are based on measurements of different thicknesses/lengths of a CL on different substrates. Suitability of the proposed methods is confirmed through a set of microstructural properties measurements on a typical CL design to ensure the measured CLs would be representative of CLs in a real fuel cell product. Conductivity measurements of two CL designs with different compositions and microstructures confirm capability of the developed procedures to track structural changes in CLs. The present characterization platform is not limited to CLs and may be used for other composite porous materials with similar structures.

Keywords: Catalyst Layer, Electronic Conductivity, Fuel Cells, Hot-pressing, Microstructure, Polymer Electrolyte Membrane Fuel Cell, Substrate, Thermal Conductivity, Thin Films

1 Introduction

Polymer electrolyte membrane fuel cells (PEMFCs) are electrochemical engines, providing electricity by reacting hydrogen with oxygen through two half-reactions occurring inside two respective catalyst layers (CLs). Other products of the overall electrochemical reaction include water and waste heat. All the electricity generation/consumption and most of the waste heat generation modes occur inside the CLs [1–5]. One of the contributing heat transfer modes is Joule heating due to electron conduction inside the CLs, where the electrons are generated (anode) or consumed (cathode). The result is a set of highly coupled multi-physics phenomena inside the CLs, i.e., a coupling between the electrochemical reactions, transport of species, electron conduction, and heat conduction. This necessitates an in-depth knowledge of thermal and electronic conductivities of CLs for optimizing the fuel cell performance for both standard conditions and non-standard conditions such as detachment of a gas diffusion layer (GDL) from a CL, membrane damage, and GDL-less designs.

Available experimental studies on thermal and electronic conductivities of CLs [3, 6–14] have used specific substrate(s) and sample preparation techniques. Accordingly, some questions have remained unanswered, in particular, whether CLs on the substrates chosen for the *ex situ* measurements differ from CLs used in a fuel cell product. CLs of PEMFCs, manufactured for commercial use, are typically coated on a decal first (typically ethylene tetrafluoroethylene (ETFE) sheets) and then transferred onto both sides of a membrane by hot-pressing to construct the catalyst-coated membrane (CCM). The CLs are hot-pressed a second time, when the CCM is stacked with GDLs to produce the membrane electrode assembly (MEA). Desired areal platinum (Pt) loadings (μg Pt catalyst per geometric area of the MEA) can be achieved by controlling the thickness of the coating. Often, *ex situ* characterizations of CLs demand coating and, sometimes, hot-pressing different

[*] Corresponding author, mbahrami@sfu.ca

CL thicknesses on different substrates appropriate for the *ex situ* characterizations. The different thicknesses are often required for deconvoluting the CL bulk signal from parasitic signals (e.g., the substrate signal). Some instances include *ex situ* thermal and electronic conductivity tests [3, 6–14]. For these tests to be relevant, microstructure of the characterized samples should be as comparable as possible to the microstructure of the desired CL in an actual MEA. Accordingly, it is important to know whether the microstructure is influenced by changing the substrate type, hot-pressing, and the CL thickness, as these parameters are generally changed during *ex situ* characterizations as described above. Several studies can be found in literature on microstructure of CLs [14–31] and effects of hot-pressing on fuel cell performance [32–35]. However, a systematic study on the influence of substrate type, hot-pressing, and CL thickness on the microstructure and the conductivities is still needed to determine suitability of *ex situ* measurements. Further, as discussed in this paper, coating different thicknesses of a CL for *ex situ* tests (especially large thicknesses) may not be possible due to loss of structural integrity of the CL, induced by a significant number of cracks, and one may have to make different thicknesses of the CL by stacking the same thickness in a testbed to perform the *ex situ* tests. For this reason, there has been this uncertainty as whether such stacking could compromise capability of *ex situ* methods to track changes in the CL microstructure, as stacking usually entails introduction of unwanted or parasitic resistances (e.g., substrates and contact resistances) into measurements. Accordingly, the main challenges in *ex situ* measurements of CLs stem from their very small thickness and fragile structure as well as the different contact resistances which may be effective in such measurements.

This work provides systematic procedures for measuring through-plane thermal and in-plane electronic conductivities of CLs with low uncertainty along with further confirmation regarding suitability of the proposed methods from a microstructural point of view. Further, the developed procedures are tested in a case study on two different CL designs with different compositions and microstructures, to confirm their capability in tracking microstructural changes. This study also addresses the need of PEMFC industry for "standardization" of test results for CLs. Currently, there is no standard for such *ex-situ* characterizations of the conductivities, and PEMFC manufacturers compare the conductivity values reported by their suppliers against other suppliers to pick a desired material. As a continuation of our previous work [6, 14], this paper is an attempt to establish such testing protocols which could be used by both the suppliers and the manufacturers.

2 Experimental Procedure

Properties investigated in the microstructural study include: thickness normalized by areal Pt loading (a measure of CL homogeneity), porosity, pore size distribution (PSD), crack density, surface roughness, and surface chemistry. In the following, procedures for measuring these properties and the conductivities are explained.

2.1 CL Fabrication

Two different catalyst inks with ionomer-to-carbon (I-to-C) weight (wt) ratios of 0.9 and 1.1 and 50 wt.% Pt in Pt-C catalyst (carbon-supported platinum) were coated in different thicknesses on ETFE and aluminum (Al) substrates.

An explanation is needed here regarding the usage of different substrates for different tests. In this study, both ETFE and Al substrates were used to measure the through-plane thermal conductivity, but only the ETFE substrate was used to measure the in-plane electronic conductivity because using Al for in-plane tests was not possible. To explain more, the very small electronic resistance of the Al substrate is in parallel to the much larger electronic resistance of the CL in in-plane tests. Thus, if an in-plane electronic resistance test is conducted on a strip of sample with CL on Al substrate, almost all the electrons will pass through the much smaller parallel resistance of the Al substrate instead of the CL. This results in only measuring the Al substrate (instead of the CL) in such tests.

Table 1 shows details of the different designs made from these inks together with their properties. The Pt-C powder used for I-to-C of 0.9 was dry ball-milled (or in short dry-milled) for 48 h to compact the Pt-C catalyst particles and reduce the porosity. Ball milling has been extensively used in literature to change the microstructure of graphitic materials [36–44]. In this process, the material is mechanically grinded by steel or, more commonly, zirconia balls in a ball mill with a rotation speed of ~60–900 rpm for a desired length of time. Within the first half hour of ball milling of carbon blacks, a maximum level of breakdown occurs for all the particles, and further ball milling leads to new bonding between the particles and compacting the microstructure [44, 45]. Ball milling of graphitic materials may also lead to bending graphitic sheets and producing onion/arch-like structures [36, 38] and, specifically, shape transition of carbon blacks from polyhedron to sphere [41].

The inks were prepared by mixing the (unmilled and ball-milled) Pt-C powders with water, solvent, and ionomer and then coated onto one side of ETFE sheets and Al foils using a Mayer bar coater (see [6] for more details about the Mayer bar coater). Different thicknesses were made using coating rods with different grades. The coatings were then dried at 55 °C on a hot plate. Design A (see Table 1) was arbitrarily chosen to

Table 1   Two different CL designs made for this study.

CL design	I-to-C ratio	Dry milling time / h	Porosity / %	Crack density / %
A	1.1	0	65 ± 2	6 ± 1
B	0.9	48	32 ± 5	16 ± 1

study the influence of the CL thickness, substrate type, and hot-pressing on the microstructure. Half of the samples of design A were kept fresh, and half of them were hot-pressed at 1.5 MPa and 150 °C for 3 min.

2.2 Areal Pt Loading Measurements

An X-ray fluorescence (XRF) analyzer (Themo Scientific, Niton XL3t) was used in a shielded test stand to measure areal Pt loadings of the samples. During a test, the analyzer emits X-rays toward the target area of the sample and receives and analyzes characteristic X-rays emitted from the excited region. The analyzer detects each element by measuring its characteristic X-ray spectrum and determines concentration of each element by counting the number of signals occurring at the energy emitted by the element.

2.3 Thickness and Porosity Measurements

Two different methods were used to measure the thickness and porosity for cross-checking: (i) scanning electron microscopy (SEM) using a Philips XL30 Environmental SEM (see [6] for more details on the method) to measure the thickness, which was also used to calculate a theoretical porosity using the known densities of the components and the areal Pt loading (see [12] for details of the calculations), and (ii) a buoyancy method similar to the technique introduced in [46] for measuring GDLs. The results from the two methods were in good agreement.

2.4 PSD Measurements

A transmission electron microscope (FEI Tecnai Osiris S/TEM) was used to measure pore size distribution (PSD) of CL samples prepared by embedding small pieces of CLs (on their substrates) in TTE resin (trimethylolpropane triglycidyl ether and 4,4'-methylenebis (2-methylcyclohexylamine)), microtoming thin (~100–200 nm) TEM slices using a Leica Ultracut UCT ultramicrotome (Leica Microsystem, Vienna, Austria), and depositing the TEM slices on 100-mesh Cu TEM grids. The imaging was performed on the samples' cross sections, with 200 kV accelerating beam voltage, by scanning a focused electron beam in a raster and collecting the signal by a high angle annular dark field (HAADF) detector. Several TEM images in different regions of a sample were collected and analyzed. TEM imaging was chosen as the technique to obtain images for measuring the PSDs because not only did it offer results which were comparable to a typically used 3D focused ion beam SEM (3D FIB-SEM), as tried by the authors for some samples, but it also proved to be a faster approach through which a larger number of areas could be imaged in a shorter time. The images were thresholded and analyzed using Fiji ImageJ software (available in the public domain) to measure the pore sizes.

2.5 Crack Density Measurements

For measuring the crack density, samples were mounted on SEM stubs, and surface images of the CLs were taken by SEM. The images were then thresholded and analyzed by the Fiji ImageJ software to obtain fraction of the total area covered by cracks.

2.6 Surface Roughness Measurements

Surface roughness was measured by a laser microscope (Keyence VK-9500K Color 3D Profile Measurement Microscope), performing measurements based on penetration of a laser beam into roughness valleys. Flatness of the samples was ensured by mounting them on glass slides. The beam scanned a CL surface at different depths of the valleys, and surface roughness was obtained from postprocessing the reflection data coming from different depths.

2.7 Surface Chemistry

X-ray photoelectron spectroscopy (XPS) was used to evaluate the surface composition at the top surface of the CL, using a Kratos Axis Ultra XPS instrument. During an XPS test, the target material is bombarded with X-rays, knocking out electrons of the sample's surface from, their chemical bonds. The XPS instrument analyzes photoelectrons emitted from the first 10 nm depth of the sample's surface due to the relatively low 0–1,200 eV excitation energy applied in these tests. Thus, XPS tests are highly surface sensitive, making them suitable for surface chemistry analysis.

In this study, broad survey scans, whose energy ranged from 1,200 to 0 eV, were performed to determine the surface composition. Using data from a survey scan, the following information could be obtained from the XPS signal: (i) atomic percentages of the elements in the CL, i.e., fluorene (F), carbon (C), sulfur (S), platinum (Pt), and oxygen (O), using areas of peaks from the broad survey scan, and (ii) weight percentages of the elements using the atomic percentages and molecular weights of the elements.

2.8 Through-plane Thermal Conductivity Measurements

In a separate study [6], we measured through-plane thermal conductivity of a CL using: (i) a custom-made guarded heat flow (GHF) device, as per ASTM Standard E1530-11 [47], and (ii) a modified transient plane source (TPS) method for thin films on a hot disk TPS 2500 S thermal constants analyzer, as per [48]. Details of these methods are given in [6, 48]. A special stacking method was used for mounting the samples in the testbeds, where two samples were made in contact from their catalyst sides, as shown in Figure 1a. This stacking method could protect the fragile CLs and enhance the signal-to-noise ratio. In short, measuring a stack of samples yields a total through-plane resistance expressed as:

$$R_{tot} = R_{b,cl} + R' = \frac{t_{cl,tot}}{k_{cl}A_{sen}} + R' \qquad (1)$$

where $R_{b,cl}$ is the bulk resistance of the CLs in the stack, and R' is the summation of all the resistances except for bulk of the CLs, i.e., substrates, probe in case of TPS tests [48], and thermal contact resistances (TCRs) in between; $t_{cl,tot}$ is the total thickness of the CLs in the stack; k_{cl} is the through-plane thermal conductivity of the CL, and A_{sen} is the area of the sensor(s) in contact with the stack. Eq. (1) shows that R_{tot} is a linear function of $t_{cl,tot}$. Therefore, by measuring stacks with multiple $t_{cl,tot}$'s, k_{cl} and R' can be deconvoluted from a linear regression analysis of the R_{tot} versus $t_{cl,tot}$ plot (k_{cl} from the slope and R' from the intercept). This requires that k_{cl} and R' remain constant by changing $t_{cl,tot}$. From the linear relationship of R_{tot} versus $t_{cl,tot}$, it can be concluded that, if we measure R_{tot} for different $t_{cl,tot}$'s and find out that the ($t_{cl,tot}$, R_{tot}) data points fall on a line, then according to Eq. (1), k_{cl} and R' must have remained constant. However, since a line can always be fitted through two points, measuring R_{tot} for just two $t_{cl,tot}$'s cannot show this linearity effectively. Accordingly, measurements of R_{tot} for stacks with more than two $t_{cl,tot}$'s should be performed. A complication which may arise is, that, to have the same microstructure, the thickness (or only areal Pt loading) of a CL can be increased to a certain limit. Beyond that limit, too much cracks are produced in the CL, and the CL may even flake off from its substrate. This limit was determined to be corresponding to a Pt loading of ~550 μg cm^{-2} for the CLs used in this study. On the other hand, small increments in the CL thickness may result in R_{tot}'s for single stacks which are too close to each other to be captured distinctively by the testbeds. Accordingly, by single-stack measurements, revealing the linear trend of R_{tot} versus $t_{cl,tot}$ in an effective way is again compromised. It is worthy to emphasize that a single stack in this context is defined as two catalyst-coated substrates made in contact from their catalyst sides, as shown in Figure 1a; thus, one stack contains two CL samples.

Figure 2 shows data points of single-stack measurements logged by the TPS and GHF testbeds. TPS samples were coated on ETFE substrates (~100 μm thick with a thermal conductivity of ~0.17 W m^{-1} K^{-1} [48]) and GHF samples on Al substrates (~50 μm thick with a thermal conductivity of ~205 W m^{-1} K^{-1}). As shown in Figure 2, the data points of single-stack measurements by each testbed fall too close to and within the uncertainty ranges of one another, based on which a resolution of ~1–2 μm in terms of the CL thickness can be obtained for the testbeds. The total resistance data from the two methods are far from each other mainly because the TPS data were taken for CLs coated on the ETFE substrates, and these substrates are considerably more thermally resistant than the Al substrates used in the GHF tests. Further, as explained in [48], TPS data also includes bulk and contact resistances inside the TPS sensor. In other words, the total thermal resistance data from the TPS and GHF tests not only contain the thermal resistance of the CLs but also contain additional resistances (substrates + contacts) which are different in TPS and GHF measurements.
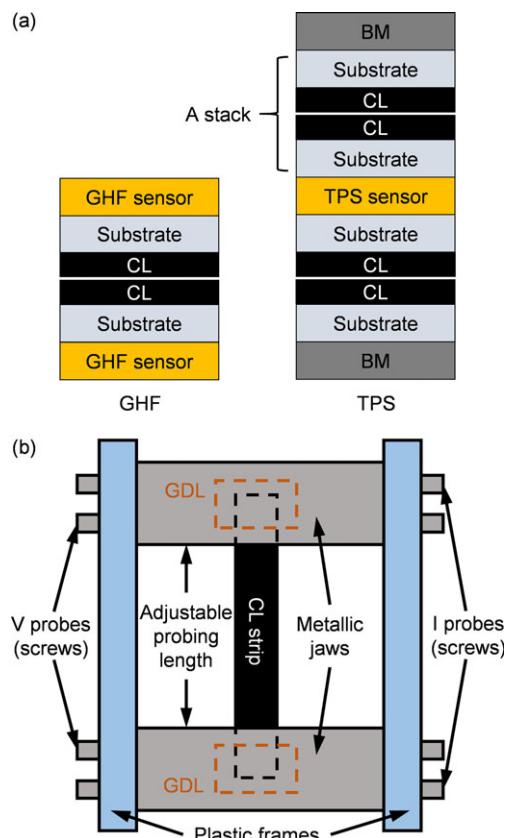

Fig. 1 Schematics of sample-sensor(s) configuration for: (a) through-plane thermal resistance tests (BM in the TPS schematic: acronym for background material), and (b) in-plane electronic resistance tests.

That is why the total thermal resistance data of Figure 2 from these methods are different. However, as will be shown later in Figure 8a, the thermal conductivity data of these methods for the same CL design (after deconvolution) are the same.

Thus, enhancing the signal-to-noise ratio is of paramount importance to: (i) effectively show the linearity of R_{tot} versus $t_{cl,tot}$, and (ii) enable measuring the CL conductivity where there are limitations to considerably change the CL thickness (due to issues with cracks and flaking).

Two possible solutions are:

(i) Fixed number of stacks (n stacks) and different thicknesses: In this method, signal from the CL bulk is enhanced by measuring more than one stack at a time (e.g., three stacks), where the number of stacks (n) is fixed, and the bulk signal is changed by changing thicknesses of CLs in each stack to enable deconvolution of the bulk conductivity by linear regression. Figure 2 shows results for the case of single stack ($n = 1$) and different thicknesses. This method mathematically ensures complete deconvolution of all the parasitic resistances from the bulk conductivity. In this case, the relation for R_{tot} remains the same as Eq. (1); only, $t_{cl,tot}$ represents the total thickness of the CL samples in all the stacks (with two CL samples per stack), and R' represents the summation of all the resistances except for the bulk of the CLs (i.e., all the substrates, probe in case of TPS tests
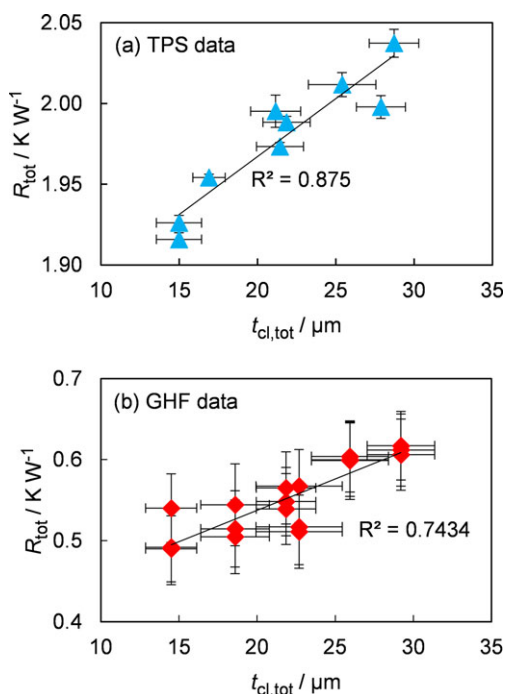
Fig. 2 Single-stack measurements of total thermal resistance *versus* total CL thickness (design A) at 1,500 kPa contact pressure and 29 °C by: (a) modified TPS method for CL on ETFE, and (b) GHF method for CL on Al, showing a resolution of ~1–2 µm CL thickness for resolving the CL resistance by the testbeds.

[48], and TCRs in between). Since a fixed number of stacks are measured and only thicknesses of the CLs in the stacks are altered, R' remains constant in this method. Accordingly, k_{cl} and R' can be found just like the single-stack measurements from the slope and intercept of the R_{tot} *versus* $t_{cl,tot}$ plot, respectively. The only difference in this case compared to single-stack measurements is that here we have a higher signal from the bulk of the CL, i.e., $n \times t_{cl,single\ stack}/(k_{cl,tp}A_{sen})$ instead of $t_{cl,single\ stack}/(k_{cl,tp}A_{sen})$.

(ii) Different numbers of stacks: In this method, signal from the CL bulk is enhanced by adding more stacks in successive measurements, where stacks with the same or different CL thicknesses can be used. This method does not mathematically guarantee complete deconvolution of parasitic resistances from the bulk conductivity. However, experiments show its promising capabilities not just for CLs in this study but also for other materials like GDLs which may not be available in different thicknesses due to manufacturing limitations [49–53]. Again, the relation for R_{tot} remains the same as Eq. (1); similar to "n-stack" measurements (fixed n), $t_{cl,tot}$ represents the total CL thickness in all the stacks and R' the rest of the resistances (i.e., all the substrates, probe in case of TPS tests [48], and TCRs in between). The only difference is that, previously, n was fixed and t_{cl} in each stack was changed to alter the CL bulk signal in "n-stack" measurements, whereas, here, t_{cl} of each stack is fixed and n is changed to alter the signal (t_{cl} may also be changed). Therefore, since the number of

stacks is different for each test, there is a risk that R' be different as well due to the difference in the number of substrates and the TCRs in between, in which case, deconvolution of k_{cl} and R' from Eq. (1) may not be possible anymore.

In the results section, justifications for the above mentioned methods are presented. Figure 3 shows schematics of the different signal enhancement methods used in this work.

2.9 In-plane Electronic Conductivity Measurements

In-plane electronic conductivity tests were performed by a Micro Junior 2 micro-ohm meter (Raytech, USA) on CL samples coated on ETFE, using a DC current. Each sample was cut into a strip and clamped inside a custom-made in-plane sample holder, shown schematically in Figure 1b. The sample holder was then connected to current and voltage leads of the ohm meter in a four-probe configuration. GDLs were used between the clamps and the sample to reduce the electronic contact resistances (ECRs) in the setup and to protect the fragile CL surfaces from the metallic jaws of the sample holder. GDLs were found to have a significantly lower resistance than the CLs (orders of magnitude lower), which would fall into the uncertainty range of the tests and could be neglected. Therefore, the total in-plane resistance of a sample, measured int this way, can be expressed as:

$$R_{tot} = R_{b,cl} + ECR = \frac{L_{cl}}{\sigma_{cl} \cdot t_{cl} \cdot W_{cl}} + ECR \qquad (2)$$

(a) A fixed number of stacks and different thicknesses
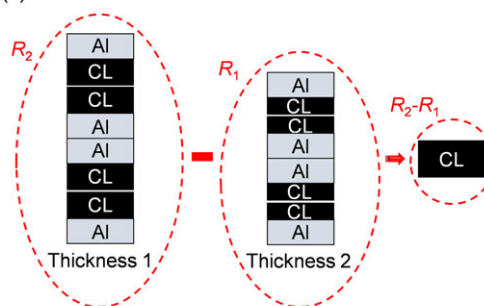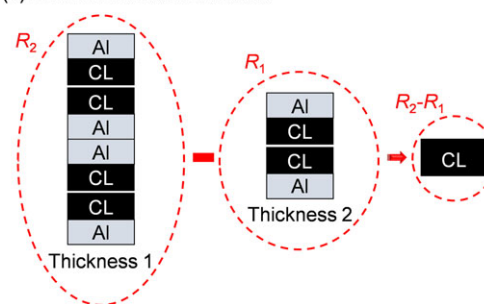
(b) Different numbers of stacks

Fig. 3 Schematics showing signal enhancement methods for measuring through-plane bulk thermal resistance (or conductivity) of CLs: (a) measuring a fixed number of stacks and only altering the CL thickness in each stack, and (b) measuring different numbers of stacks using the same CL thickness in each stack and only altering the number of stacks in the tests.

where $R_{b,cl}$ is the bulk resistance of the CL; *ECR* represents any miscellaneous ECRs in the measurement; σ_{cl} and t_{cl} are in-plane conductivity and thickness of the CL, respectively, and L_{cl} and W_{cl} are the probed length (distance between the sample holder clamps) and width of the CL strip, respectively. Similar to the above-mentioned discussions for through-plane thermal conductivity tests, if σ_{cl} and *ECR* remain constant by changing L_{cl}, Eq. (2) will indicate a linear relationship between R_{tot} and L_{cl}, whose slope and intercept can be used to find σ_{cl} and *ECR*, respectively.

3 Results and Discussion

3.1 Assessment of the Conductivity Measurement Procedures

3.1.1 Microstructural Study

Measurements showed that various microstructural properties did not change with CL thickness, substrate type, and hot-pressing. For conciseness, average values of all the tests are summarized in Table 2 for normalized thickness (CL thickness normalized by its areal Pt loading), porosity, crack density, and surface roughness. Distributions of pore sizes and surface chemical elements are shown in Figure 4.

The 0.002 $\mu m\ \mu g^{-1}$ standard deviation of the normalized thickness in Table 2 is small compared to the normalized thickness value of 0.0324 $\mu m\ \mu g^{-1}$ (i.e., only ~6% of the normalized thickness). This shows that changing the CL thickness did not change the normalized thickness significantly, and thus indicates good homogeneity of the CLs in terms of dispersion of Pt particles across the thickness.

As shown in Table 2, the measured crack densities for all the samples of design A were around 6% and within the uncertainty ranges of one another; uncertainty in this context refers to standard deviation of the measurements. However, larger cracks were observed for higher CL thicknesses, as shown in Figure 5. This could be a result of slower drying of higher amounts of catalyst ink (when coating a higher CL thickness) due to higher thermal resistance of the thicker ink, which could give the coating enough time to develop larger cracks as it dried. As resistance of cracks is in parallel with the CL bulk resistance in through-plane tests, the difference in crack sizes was not expected to affect the through-plane thermal conductivity results. As shown later, the collected thermal conductivity data from different thicknesses also showed this advantage. However, as resistance of cracks is in series with the CL bulk resistance in in-plane tests, one should be wary of

Table 2 Microstructural properties for design A averaged over cases with different CL thicknesses, substrates (ETFE and Al), and hot-pressing states (fresh and hot-pressed).

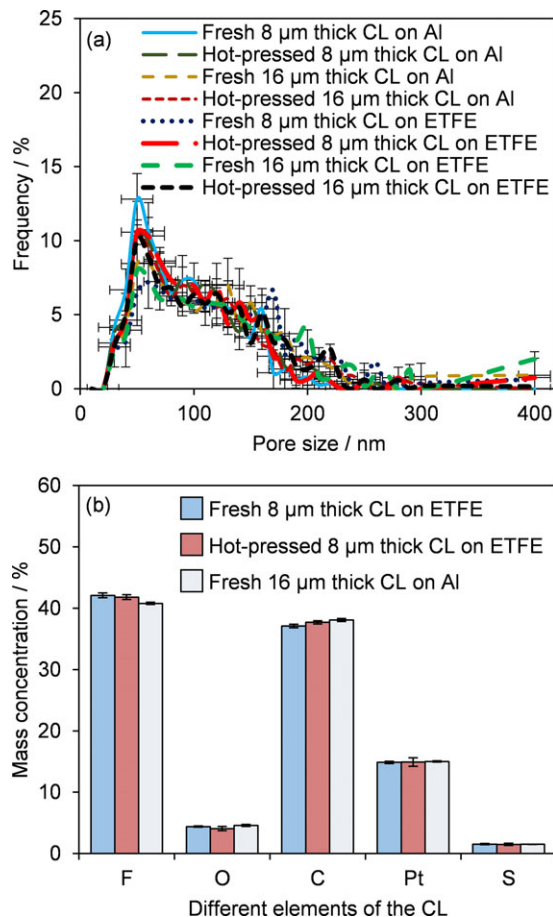| Microstructural property	Normalized thickness / $\mu m\ \mu g^{-1}$	Porosity / %	Crack density / %	Surface roughness / μm
Measured value	0.0324 ± 0.002	65 ± 2	6 ± 1	0.68 ± 0.04

Fig. 4 Distribution of: (a) pore sizes measured by TEM imaging, and (b) surface chemical elements measured by XPS, for CL samples from design A with different thicknesses, substrates, and hot-pressing.
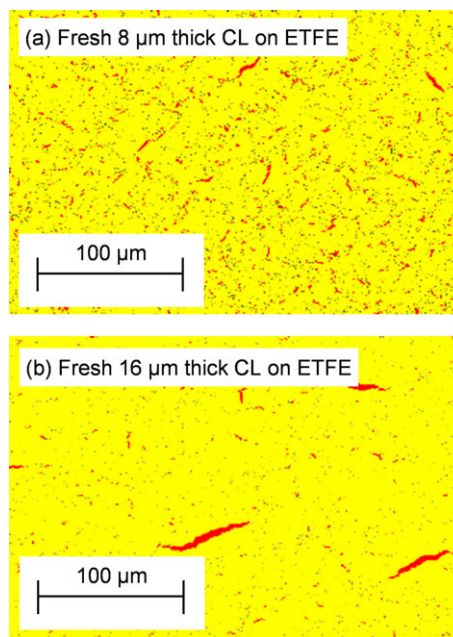

Fig. 5 Processed SEM surface images of CL samples from design A (red: crack) for: (a) an 8 μm thick CL on ETFE, and (b) a 16 μm thick CL on ETFE, showing formation of larger cracks by increasing the coating thickness.

this situation when using different CL thicknesses for in-plane tests. Considering that in-plane tests do not need different thicknesses, but instead need different lengths of a CL for data reduction, one can simply avoid the risk by using the desired CL thickness for in-plane tests. Further, this issue may not affect the in-plane tests, if crack densities of different thicknesses are small and close to each other, as shown later for design A. On the other hand, when coating a higher CL thickness was tried for design A (i.e., higher than ~16 μm), density of large cracks significantly increased and led to flaking off the CL from its substrate. Accordingly, one can say that the highest achievable thickness for this CL (design A), which could hold its structural integrity, was ~16 μm.

The PSDs in Figure 4a show the same pattern and indicate insignificant effects from the CL thickness, substrate type, and hot-pressing, within the error range. Further, on average, more than 90% of the resolved pores had a size smaller than 180 nm, and there was no pore larger than 400 nm. Two interesting observations can be made by comparing the PSDs in Figure 4a with results of N_2 adsorption porosimetry for CLs with similar compositions from [24, 54]. First, the N_2 adsorption results of [24, 54] do not show pore sizes larger than 100 nm, whereas the TEM image analysis of this work could find pores close to 400 nm. This difference could be due to the very different natures/principles of these measurement techniques and demands a more in-depth investigation of the underlying roots, which is not in the scope of this work and is suggested as a future work. Another interesting observation is that despite these differences, both techniques yielded a peak size of around 50 nm.

As shown in Figure 4b, surface composition did not change either by CL thickness, substrate type, or hot-pressing. Hydrogen (an element of the ionomer) is absent in the results because it cannot be detected by XPS due to participation of its single valence electron in chemical bonding [55].

In summary, except for crack sizes, the CL microstructure did not change with hot-pressing, substrate type, or CL thickness. The issue with different crack sizes may only affect the in-plane conductivity of CLs with high crack density, and it can simply be avoided by selecting the desired thicknesses for those tests. Thus, from a

microstructural point of view, the developed conductivity measurement procedures are directly applicable for CLs in a real fuel cell product.

3.1.2 Benchmarking the Through-plane Thermal Conductivity Tool

Figure 6 compares raw and post-processed data for the methods of "$n = 1$ stack and different thicknesses", "$n = 3$ stacks and different thicknesses", and "different numbers of stacks" (with the same CL thickness in the stacks and n up to 6 here) for fresh CLs on Al using the GHF testbed. As indicated by the R-squared values in the R_{tot} versus $t_{cl,tot}$ plots (Figures 6a and 6b), the methods of "$n = 3$ stacks and different thicknesses" and "different numbers of stacks" are significantly more capable of enhancing the signal from the CL bulk and capturing the linearity of the data than the method of "$n = 1$ stack and different thicknesses". This higher capability
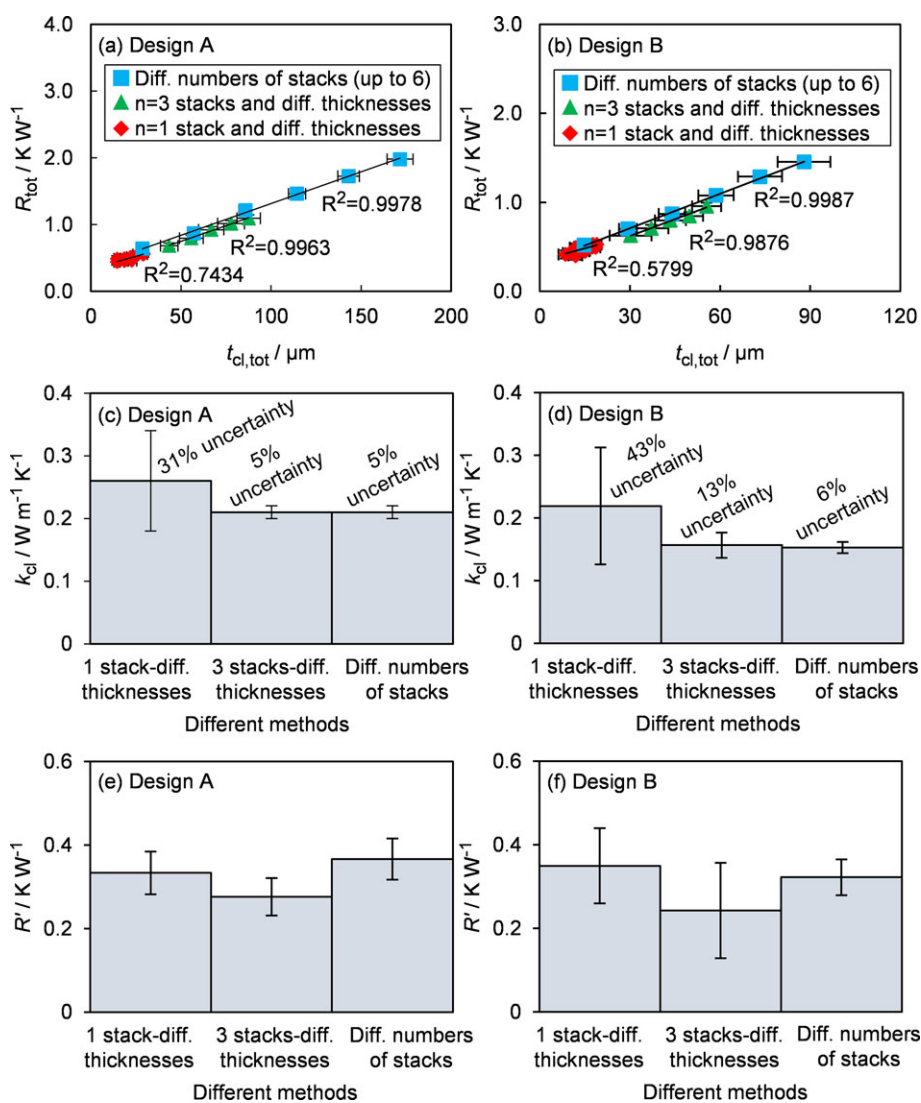

Fig. 6 Through-plane thermal tests of fresh CLs on Al using the GHF testbed at 1,500 kPa contact pressure and 29 °C: (a, b) total resistance versus total CL thickness, (c, d) deconvoluted thermal conductivities, and (e, f) deconvoluted parasitic resistances.

is reflected in the significantly lower uncertainties of the conductivity data deconvoluted by those methods, as shown in Figures 6c and 6d. Further, the method of "different numbers of stacks" seems to be more capable of enhancing the signal-to-noise ratio than the method of "$n = 3$ stacks and different thicknesses", as in this method, one can enhance the signal simply by adding more stacks, and one does not have to have different thicknesses of the CL to do so. However, since the number of substrates and TCRs in between increases by adding more stacks, one may not expect to have the same parasitic resistance (i.e., R') for the method of "different numbers of stacks" in different tests. Justifications for applicability of this method can be understood from the parasitic resistance data plotted in Figures 6e and 6f. As indicated by overlap of the uncertainty bars in the graphs, parasitic resistance did not change statistically by adding more stacks. The reason for this observation is that TCRs between the stack-sandwich and the GHF sensors are dominant in R', such that adding more stacks (up to 6 here) did not affect this dominance and kept R' constant. Another supporting evidence regarding the dominance of the TCRs between the two end Al foils and the GHF sensors was observed when stacks of multiple bare Al substrates (each 50 μm thick) were measured and no change was observed in the total resistance by adding more samples to the stack. It seemed that the stacks of Al substrates were invisible to the device. Further, the total resistance values measured for the stacks of bare Al substrates had the same magnitude as the parasitic resistances deconvoluted from the stacks of CL samples, shown in Figures 6e and 6f. This further confirms that the CL samples as well as the Al foil samples must have had good internal thermal contacts in the stacks, which led to such small internal TCRs in the stacks that could not be captured by the testbed. This was repeatedly observed in measurements of other CL designs with different structures.

Agreement of the last two columns of Figures 6c and 6d shows that the through-plane thermal conductivity does not change with CL thickness. Further, as mentioned before, the method of "different numbers of stacks" is generally more efficient than the method of "$n = 3$ stacks and different thicknesses" in terms of uncertainty of the deconvoluted thermal conductivity, and it also has the advantage of enabling measurements with just one thickness of a CL, where there are limitations for increasing the CL thickness, e.g., where structural integrity of the CL may be compromised by development of cracks and subsequent flaking. However, it should be emphasized that the validity of the method of "different numbers of stacks" was confirmed here just for 1,500 kPa contact pressure (and higher). One should be cautious when using this method at lower pressures, as the effects of TCRs may no longer be negligible at lower pressures. In this work, there was no need for confirming validity of the method for lower pressures, as thermal conductivity of CLs does not change much with pressure [5, 6]. Besides, this method is applicable for the entire ~1,500–3,000 kPa working pressure range of fuel cells.

3.1.3 Benchmarking the In-plane Electronic Conductivity Tool

Figure 7 shows raw and post-processed data for in-plane electrical tests of fresh CLs on ETFE. As R-squared values of the fitted lines show in Figure 7a, R_{tot} changes very linearly with L_{cl} for both designs, proving that σ_{cl} and ECR remained constant by changing L_{cl}. This allowed deconvolution of σ_{cl} and ECR for each case from the slope and intercept of the relevant R_{tot} versus L_{cl} plot, respectively, as shown in Figures 7b and 7c. Comparing the parasitic ECR values in Figure 7c with the typical total resistance values in Figure 7a reveals small order of magnitude of the ECR compared to the total resistance. This is ideal and leads to small uncertainties for the deconvoluted conductivity data, as shown in Figure 7b. The major sources of uncertainty in σ_{cl} are, in fact, uncertainties in measurements of the thickness and length of the CL.
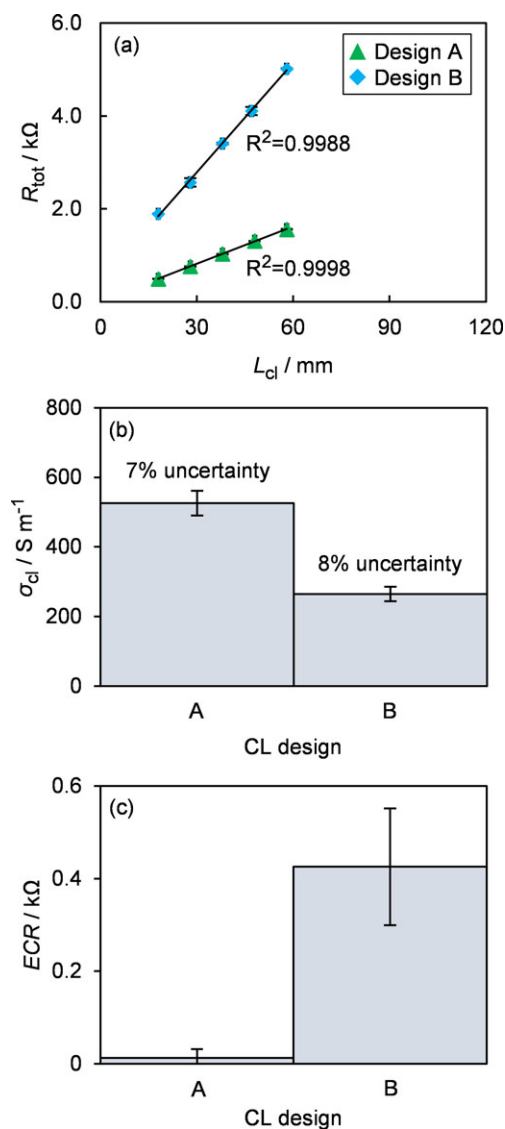

Fig. 7 In-plane electrical tests of fresh CLs on ETFE at 24 °C: (a) total resistance versus probing length, (b) deconvoluted electronic conductivities, and (c) deconvoluted parasitic resistances.

3.2 Case Studies

3.2.1 Cases with No Change in Microstructure

In the previous study [6], we found from two thickness measurements that neither the substrate type nor hot-pressing affected the through-plane thermal conductivity of design A. We also showed that both TPS and GHF testbeds agreed well with each other in [6, 48]. Figure 8 shows the conductivities for cases with different CL thicknesses, substrates, and hot-pressing but the same microstructure. In Figure 8a, conductivity data of [6] are compared with the data of "n = 3 stacks and different thicknesses" in this work. In the last column of Figure 8b, the CL was hot-pressed onto an NRE-211 Nafion membrane as another substrate for in-plane electrical measurements. As shown in Figure 8, conductivity data of the different cases agree well, which reflects the previously shown fact that CL microstructure does not change with CL thickness, substrate type, or hot-pressing. Since the in-plane electronic conductivity data for CL on ETFE were the same as those for CL on membrane, one has the flexibility of taking samples for the in-plane tests either from catalyst-coated ETFE decals or from CCMs made during the MEA production. For through-plane thermal conductivity, though, it is recommended to coat the samples on Al which has a much lower thermal resistance than polymers (such as ETFE and membranes) to have the highest signal-to-noise ratio.
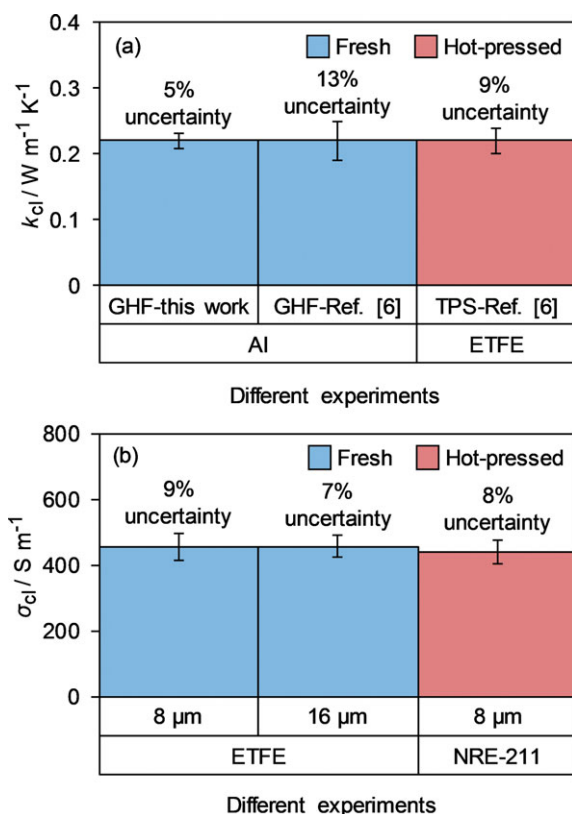
3.2.2 Cases with Different Microstructures

As indicated in the low-uncertainty data of Figures 6c and 6d, through-plane thermal conductivity of design B was less than that of A, which can be explained by effects of dry milling. As mentioned before, shape of carbon particles may go through a transition from polyhedron to sphere by dry milling the catalyst powder [41]. This leads to reduction in the size of contact areas between the particles from flat facets of polyhedrons to point contacts between spheres, hence leading to augmentation in constriction/spreading resistance through the particles and, consequently, reduction in thermal conductivity. Figure 7b shows that in-plane electronic conductivity of design B is also less than A. This may be partly a result of reduction in contact area between the carbon particles by dry milling and partly due to the much higher crack density of design B compared to A (see Table 1). High crack densities can significantly reduce the in-plane electronic conductivity because, as mentioned before, resistance of cracks is in series to the bulk CL resistance in the in-plane conduction, and in case of electron conduction, cracks are completely insulating. Further, SEM images of the CLs also showed that design B had much longer cracks than design A, which would go deep through the whole CL thickness (see Figure 9). Accordingly, development of long, deep cracks plays a major role in the low in-plane electronic conductivity of design B. This crack development is itself a direct result of: (i) weak structural integrity of design B due to its low ionomer content (i.e., low I-to-C ratio) and, hence, less ionomer as a binder, and (ii) smaller and, hence, weaker connections between the carbon particles of design B by dry milling due to the subsequent shape transition.

Fig. 8 Conductivity data for CLs with the same microstructure: (a) through-plane thermal conductivity (''GHF-this work'' by the method of ''n = 3 stacks and different thicknesses''), and (b) in-plane electronic conductivity.
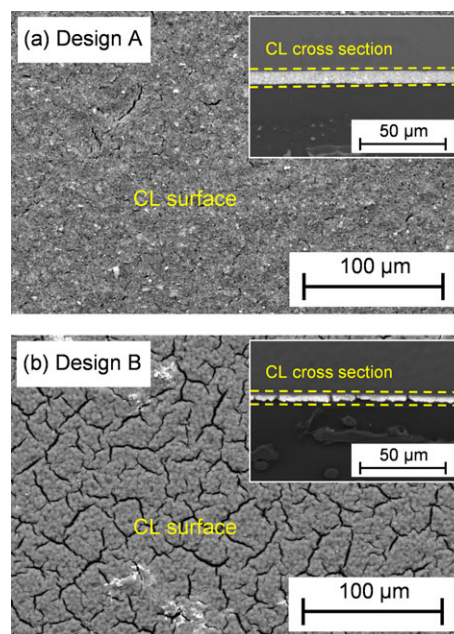

Fig. 9 Surface and cross-sectional SEM images of: (a) design A, and (b) design B, showing the very different microstructures of these designs.

One point is worth mentioning regarding the SEM surface images of Figure 9. The SEM images were acquired using the backscattered electron (BSE) detector. Since heavy elements (i.e., elements with high atomic numbers) backscatter electrons more strongly than light elements (i.e., elements with low atomic numbers), heavy elements appear brighter in SEM images. Thus, the white marks observed on the surface of design B in Figure 9b are, in fact, made of the heavy element Pt. This shows that, for design B, some Pt particles were removed from the carbon support by long dry milling (for 48 h) and made localized Pt aggregates (i.e., the white marks in Figure 9b). On the other hand, as can be observed from Figure 9a, design A with 0 h dry milling time did not show this effect. As also mentioned in [18,56], such Pt detachment leads to loss of electrochemical surface area, and thus lower catalytic activity, which is detrimental to fuel cell performance. Thus, aggressive dry milling of the catalyst powder is not desirable in general.

Overall, we can conclude that the developed conductivity measurement procedures are capable of tracking changes in the microstructure. Another interesting point is that design B had the lowest conductivities despite having the lowest porosity (see Table 1), which is counterintuitive. This shows that the common notion that lower porosity should lead to higher conductivity may not be valid due to effects of other structural parameters, such as particle shape and cracks in the cases studied here. Accordingly, studies of structure-property correlations are of paramount importance to achieve a fundamental understanding of the material's behavior. The conductivity measurement procedures proposed in this work provide tools for such studies.

4 Conclusions

In this work, testing protocols with low uncertainties were proposed for standardizing measurements of through-plane thermal and in-plane electronic conductivities of CLs. The proposed methods involved coating different CL thicknesses/lengths on different substrates with or without hot-pressing. The proposed methods were shown to be suitable and relevant for CLs in a real product by confirming: (i) the same microstructure and conductivities for CLs with different thicknesses, substrate types, and hot-pressing, (ii) high signal-to-noise ratio of the procedures, and (iii) satisfactory deconvolution of parasitic resistances. Measurements of two different CL designs with different microstructures further confirmed the suitability of the proposed procedures in tracking microstructural changes. One interesting area for future studies would be measuring different CL designs with different types of carbon support and degradation levels, using the proposed procedures in this study, and correlating the measurements to microstructural details. The characterization platform developed in this work is not limited to CLs and can be extended to other composite porous materials with the same measurement challenges and complexities.

List of Symbols

Symbols and Variables

A	Surface area / m^2
ECR	Electronic contact resistance / Ω
k	Thermal conductivity / W m^{-1} K^{-1}
L	Length / m
R	Resistance, K W^{-1} if thermal, and Ω if electronic
R'	A constant parasitic thermal resistance / K W^{-1}
t	Thickness / m
W	Width / m

Greek Letters

σ	Electronic conductivity / S m^{-1}

Subscripts

b	Bulk
cl	Catalyst layer
sen	Sensor
tot	Total

References

[1] M. J. Lampinen, M. Fomino, *J. Electrochem. Soc.* **1993**, *140*, 3537.

[2] S. G. Kandlikar, Z. Lu, *Appl. Therm. Eng.* **2009**, *29*, 1276.

[3] M. Khandelwal, M. M. Mench, *J. Power Sources* **2006**, *161*, 1106.

[4] M. Bhaiya, A. Putz, M. Secanell, *Electrochim. Acta* **2014**, *147*, 294.

[5] M. Ahadi, A. Putz, J. Stumper, M. Bahrami, *J. Power Sources* **2017**, *354*, 215.

ORIGINAL RESEARCH PAPER

ORIGINAL RESEARCH PAPER

[6] M. Ahadi, M. Tam, M. S. Saha, J. Stumper, M. Bahrami, *J. Power Sources* **2017**, *354*, 207.

[7] N. Alhazmi, M. S. Ismail, D. B. Ingham, K. J. Hughes, L. Ma, M. Pourkashanian, *J. Power Sources* **2013**, *241*, 136.

[8] N. Alhazmi, D. B. Ingham, M. S. Ismail, K. Hughes, L. Ma, M. Pourkashanian, *J. Power Sources* **2014**, *270*, 59.

[9] O. S. Burheim, H. Su, H. H. Hauge, S. Pasupathi, B. G. Pollet, *Int. J. Hydrogen Energ.* **2014**, *39*, 9397.

[10] T. Suzuki, H. Murata, T. Hatanaka, Y. Morimoto, *R&D Rev. Toyota CRDL* **2003**, *39*, 33.

[11] P. Gode, F. Jaouen, G. Lindbergh, A. Lundblad, G. Sundholm, *Electrochim. Acta* **2003**, *48*, 4175.

[12] D. R. Morris, S. P. Liu, D. Villegas Gonzalez, J. T. Gostick, *ACS Appl. Mater. Inter.* **2014**, *6*, 18609.

[13] C. Du, P. Shi, X. Cheng, G. Yin, *Electrochem. Commun.* **2004**, *6*, 435.

[14] M. Ahadi, M. Tam, J. Stumper, M. Bahrami, *Int. J. Hydrogen Energ.* **2019**, *44*, 3603.

[15] M. Uchida, Y. Aoyama, N. Eda, A. Ohta, *J. Electrochem. Soc.* **1995**, *142*, 4143.

[16] M. Uchida, Y. Fukuoka, Y. Sugawara, N. Eda, A. Ohta, *J. Electrochem. Soc.* **1996**, *143*, 2245.

[17] R. Fernandez, P. Ferreira-Aparicio, L. Daza, *J. Power Sources* **2005**, *151*, 18.

[18] K. More, R. Borup, K. Reeves, *ECS Trans.* **2006**, *3*, 717.

[19] H. M. Yu, C. Ziegler, M. Oszcipok, M. Zobel, C. Hebling, *Electrochim. Acta* **2006**, *51*, 1199.

[20] P. P. Mukherjee, C. Y. Wang, *J. Electrochem. Soc.* **2006**, *153*, A840.

[21] K. Malek, M. Eikerling, Q. Wang, T. Navessin, Z. Liu, *J. Phys. Chem. C* **2007**, *111*, 13627.

[22] Z. Yu, R. N. Carter, *ECS Trans.* **2009**, *19*, 1.

[23] T. Sobolyeva, *Ph.D. Thesis*, Simon Fraser University, Vancouver, Canada, **2010**.

[24] T. Soboleva, X. Zhao, K. Malek, Z. Xie, T. Navessin, S. Holdcroft, *ACS Appl. Mater. Inter.* **2010**, *2*, 375.

[25] K. Malek, T. Mashio, M. Eikerling, *Electrocatal.* **2011**, *2*, 141.

[26] H. Schulenburg, B. Schwanitz, N. Linse, G. G. Scherer, A. Wokaun, J. Krbanjevic, R. Grothausmann, I. Manke, *J. Phys. Chem. C* **2011**, *115*, 14236.

[27] P. Dobson, C. Lei, T. Navessin, M. Secanell, *J. Electrochem. Soc.* **2012**, *159*, B514.

[28] Z. Yu, R. N. Carter, J. Zhang, *Fuel Cells* **2012**, *12*, 557.

[29] S. Holdcroft, *Chem. Mater.* **2013**, *26*, 381.

[30] S. Ghosh, H. Ohashi, H. Tabata, Y. Hashimasa, T. Yamaguchi, *Int. J. Hydrogen Energ.* **2015**, *40*, 15663.

[31] M. Sabharwal, L. M. Pant, A. Putz, D. Susac, J. Jankovic, M. Secanell, *Fuel Cells* **2016**, *16*, 734.

[32] M. S. Wilson, S. Gottesfeld, *J. Electrochem. Soc.* **1992**, *139*, L28.

[33] T. A. Zawodzinski, T. E. Springer, F. Uribe, S. Gottesfeld, *Solid State Ionics* **1993**, *60*, 199.

[34] H. Tang, S. Wang, S. P. Jiang, M. Pan, *J. Power Sources* **2007**, *170*, 140.

[35] M. Yazdanpour, A. Esmaeilifar, S. Rowshanzamir, *Int. J. Hydrogen Energ.* **2012**, *37*, 11290.

[36] J. Y. Huang, H. Yasuda, H. Mori, *Chem. Phys. Lett.* **1999**, *303*, 130.

[37] Y. Chen, J. F. Gerald, L. T. Chadderton, L. Chaffron, *Appl. Phys. Lett.* **1999**, *74*, 2782.

[38] X. H. Chen, H. S. Yang, G. T. Wu, M. Wang, F. M. Deng, X. B. Zhang, J. C. Peng, W. Z. Li, *J. Cryst. Growth.* **2000**, *218*, 57.

[39] Z. Q. Li, C. J. Lu, Z. P. Xia, Y. Zhou, Z. Luo, *Carbon* **2007**, *45*, 1686.

[40] J. M. Yusof, M. A. M. Salleh, S. A. Rashid, I. Ismail, S. N. Adam, *JESTEC*, Special Issue on Applied Engineering and Sciences (SAES2013), (Eds. N. Misron, S. A. Ahmad, N. F. Mailah, C. V. Aravind), **2014**, *9*, 125.

[41] S. Zhang, Y. Cui, B. Wu, R. Song, H. Song, J. Zhou, X. Chen, J. Liu, L. Cao, *RSC Adv.* **2014**, *4*, 505.

[42] S. Li, S. Liu, Z. Fu, Q. Li, C. Wu, W. Guo, *Surf. Interface Anal.* **2017**, *49*, 197.

[43] N. Hamran, A. A. Rashid, *AIP Conf. Proc.* **2017**, *1865*, *1*, 040011.

[44] D. Leistenschneider, K. Zürbes, C. Schneidermann, S. Grätz, S. Oswald, K. Wegner, B. Klemmed, L. Giebeler, A. Eychmüller, L. Borchardt, *Journal of Carbon Research* **2018**, *4*, 14.

[45] J. B. Donnet, R. C. Bansal, M. J. Wang, *Carbon Black: Science and Technology*, 2 ed., CRC Press, New York, USA, **1993**.

[46] R. R. Rashapov, J. Unno, J. T. Gostick, *J. Electrochem. Soc.* **2015**, *162*, F603.

[47] ASTM E1530-11, ASTM International, West Conshohocken, PA, can be found under www.astm.org, **2011**.

[48] M. Ahadi, M. Andisheh-Tadbir, M. Tam, M. Bahrami, *Int. J. Heat Mass Tran.* **2016**, *96*, 371.

[49] O. Burheim, P. Vie, J. Pharoah, S. Kjelstrup, *J. Power Sources* **2010**, *195*, 249.

[50] O. S. Burheim, J. G. Pharoah, H. Lampert, P. J. Vie, S. Kjelstrup, *J. Fuel Cell Sci. Tech.* **2011**, *8*, 021013.

[51] O. Burheim, G. Ellila, J. Fairweather, A. Labouriau, S. Kjelstrup, J. Pharoah, *J. Power Sources* **2013**, *221*, 356.

[52] O. S. Burheim, H. Su, S. Pasupathi, J. G. Pharoah, B. G. Pollet, *Int. J. Hydrogen Energ.* **2013**, *38*, 8437.

[53] S. Hasanpour, M. Ahadi, M. Bahrami, N. Djilali, M. Akbari, *J. Power Sources* **2018**, *403*, 192.

[54] T. Suzuki, S. Tsushima, S. Hirai, *Int. J. Hydrogen Energ.* **2011**, *36*, 12361.

[55] N. Stojilovic, *J. Chem. Educ.* **2012**, *89*, 1331.

[56] B. G. Pollet, J. T. E. Goh, *Electrochim. Acta* **2014**, *128*, 292.